Nuclear Instruments and Methods in Physics Research A 344 (1994) 335–349
North-Holland

NUCLEAR
INSTRUMENTS
& METHODS
IN PHYSICS
RESEARCH
Section A

Design, construction and test results of the ZEUS forward tracking detector

B. Bock [1], H. Dabbous [2], B. Gutjahr [3], H. Hartmann, M. Herzog, S. Kramarczyk, B. Schneider [4], R. Wedemeyer, M. Zachara [5]
Physikalisches Institut, Rheinische Friedrich-Wilhelms-Universität, Bonn, Germany [+]

U. Schneekloth *, J. Schroeder
Deutsches Elektronen-Synchrotron, Hamburg, Germany [+]

F. Barreiro, E. Diez, F. Enríquez, S. Gallego, L. Labarga
Depto. Fisica Teórica, Universidad Autónoma de Madrid, Madrid, Spain [++]

(Received 9 December 1993)

The design and construction of the ZEUS forward tracking detector is described. The detector consists of three large planar drift chambers mounted in the forward direction with respect to the proton beam and a smaller rear detector of the same type. Test beam measurements performed at DESY show a single wire spatial resolution of 105 μm and a dE/dx resolution of 8.8%. The resolution of the three-dimensional track coordinates and slopes provided by one chamber are found to be 90 μm and 2.7 mrad, respectively.

1. Introduction

The ZEUS detector was built for studying the collisions of 820 GeV protons on 30 GeV electrons in the HERA storage ring located at DESY. The main components of ZEUS are the inner tracking detectors, which are surrounded by a 1.8 T superconducting solenoid, a high resolution depleted uranium scintillator sandwich calorimeter and a muon detection system. Good tracking in the forward region, i.e. in the proton beam direction, is of particular importance where jet topologies and the Lorentz boost result in high track densities. In the rear direction good tracking helps in identifying the scattered electron in low Bjorken x and low Q^2 interactions.

[+] This work was supported by the German Federal Ministry for Research and Technology (BMFT).
[++] This work was supported by the Spanish Ministry of Science (CICYT).

[1] Now at Krupp Atlas Electr., Bremen.
[2] Now at SAP, Heidelberg.
[3] Now at DESY, Hamburg.
[4] Now at INFAS, Bonn.
[5] Now at Institute of Nuclear Physics, Cracow, Poland.
* Corresponding author.

The inner tracking system was designed taking these considerations into account. It consists of (see Fig. 1): a vertex detector VXD (a high resolution cylindrical drift chamber), a central tracking detector CTD (a large cylindrical drift chamber), the forward tracking detector FTD (a set of three planar drift chambers) and the rear tracking detector RTD. The four planar drift chambers were added to the central tracking detector to improve the angular coverage and the track reconstruction at small and large polar angles where the wire orientation of the CTD becomes unfavorable. The forward tracking detector consists of three disklike chambers FTD1, 2, 3 (Fig. 1), each providing three-dimensional track information. The FTDs are separated by two gaps of 210 mm each, which are used to accommodate 2×2 modules of the transition radiation detector TRD.

In this paper, we report on the design and the construction of the forward tracking detector. Results on the chamber performance are presented, which were obtained using test beam data taken at DESY. In addition to the single wire spatial resolution and the resulting resolution of the three-dimensional track parameters, the energy loss measurement (dE/dx) was studied.

SSDI 0168-9002(93)E1316-P

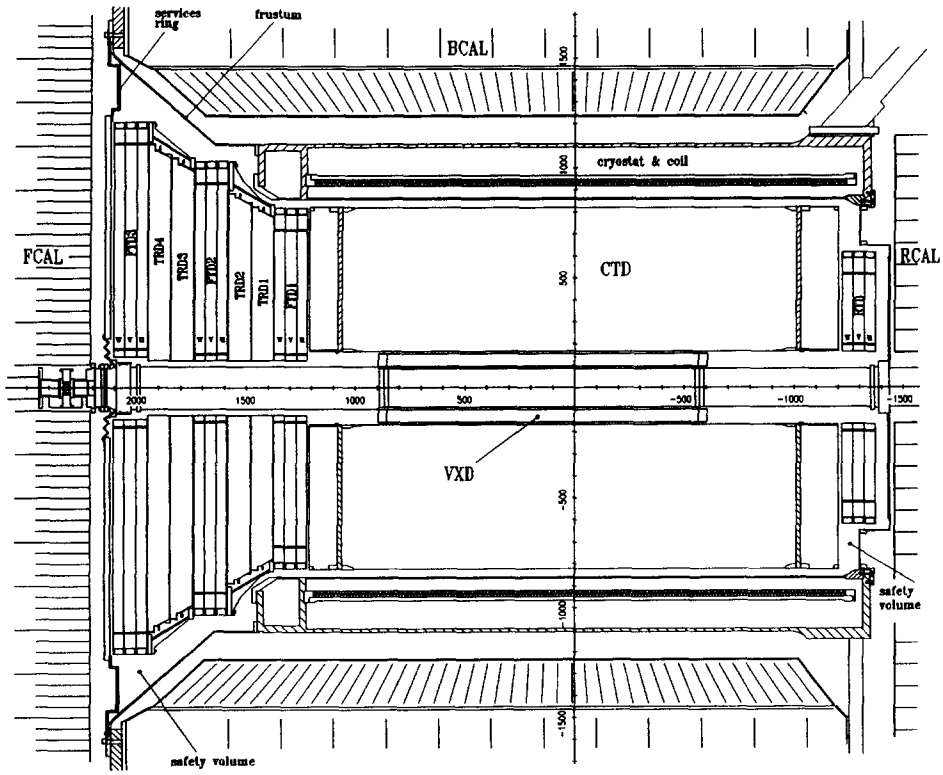

Fig. 1. Layout of the ZEUS inner detector. Vertical section.

2. Design

2.1. Chamber design

The structure of the forward tracking detector as well as the internal structure of the individual chambers were designed to meet the following general requirements:

– The redundancy in the number of digitizings per drift cell has to be sufficient to resolve the left–right ambiguity already at the cell level and to cope with inefficiencies as well as spurious hits.

Table 1
Parameters of the FTDs and RTD

Distance from collision point [mm]	FTD1	FTD2	FTD3	RTD
	1220–1374	1586–1740	1952–2106	(−1218)–(−1372)
Overall				
Inner radius [mm]	124	124	144	164
Outer radius [mm]	820	1030	1210	620
Sensitive area				
Inner radius [mm]	180	180	200	220
Outer radius [mm]	695	905	1085	495
Angular acceptance [mrad]	140–470	122–489	105–489	175- 350
Detection [deg]	80–270	70–280	60–280	100–200
Number of cells	204	252	300	168
Number of signal wires	1224	1512	1800	1008
Number of potential wires	1428	1764	2100	1176
Total number of channels		4536		1008
Gas volume [m^3]	0.25	0.40	0.60	0.14
Total gas volume [m^3]		1.39		
Radiation thickness				
Sensitive area	$0.09X_0$	$0.09X_0$	$0.09X_0$	$0.09X_0$
Outer rim	$0.13X_0$	$0.13X_0$	$0.13X_0$	$0.13X_0$

– Each chamber has to provide three independent stereo views of a track element to ease the reconstruction of three-dimensional track elements by redundant information.

– The number of measured three-dimensional track elements (i.e. the number of chambers) has to exceed the minimum of two to keep the efficiency for track finding high and to ease linking tracks seen by the forward detector to tracks seen in the CTD and the vertex detector.

Each chamber consists of three independent layers of drift cells with fixed wire orientations, rotated by 120° going from one layer to the next (Fig. 2). Each drift cell has six sense wires. Thus one chamber measures three projections (u, v, w) of a track element with up to six digitizings per projection.

The basic mechanical concept of the planar drift chambers was developed with the aim to minimize radiation thickness and, at the same time, to have a structure rigid enough to take all internal and external forces without distorting intolerably. The resulting design is summarized in Table 1.

The chamber body is a self-supporting structure made of printed circuit boards. The load of the wire tension is taken by this body structure rather than by massive frames. Each cell has its own wire mounts, which are attached to the chamber body.

External forces are introduced into a thin and hollow aluminium structure at the perimeter of the body, rigidly connected to it. Between the inner edge of the aluminium pieces and the beginning of the cells is a free space of about $\Delta r = 80$ mm. This space is needed to accommodate wire mounts, signal cables, and HV distributors. There is also a reinforcement structure at the inner (beampipe) hole of the chamber. It is made of thin pieces of glass fiber epoxy and supports cylindrical aluminium sheets, 0.5 mm thick, to close the chamber.

2.2. Cell design

A cross section of the FTD (RTD) drift cell is shown in Fig. 3. The inner dimensions are $\Delta z = 48$ mm

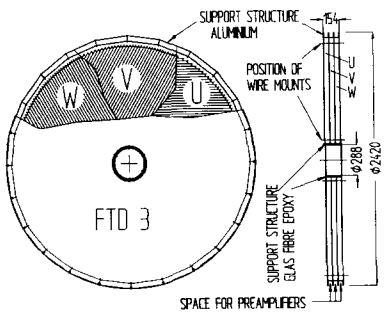

Fig. 2. Basic chamber design. FTD3 as an example.

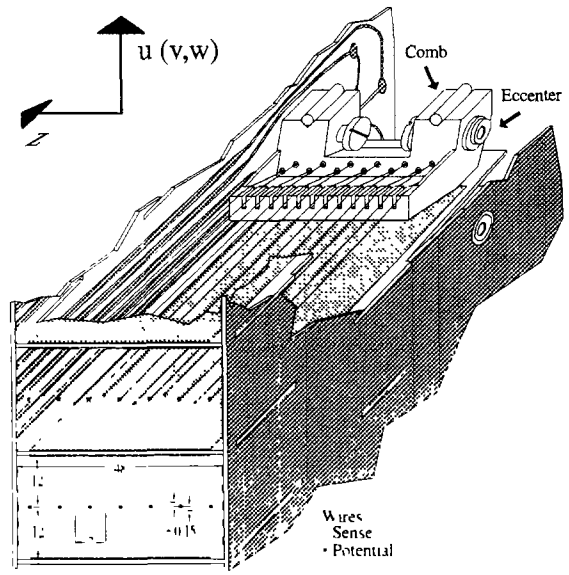

Fig. 3. Cross section and sketch of two drift cells.

and Δu (Δv, Δw) = 24 mm. Each cell contains six sense wires (30 μm diameter), spaced by 7 mm, and seven potential wires (121 μm diameter), perpendicular to the chamber axis (i.e. the beam direction). The potential wires lie in the median plane between the cathode planes. The sense wires are staggered with respect to this median plane by ±150 μm to allow a resolution of the left–right ambiguity already at the cell level. The distance of 12 mm between the median plane and the cathodes was chosen to be small enough

– to keep the maximum drift time (for extreme B-field conditions) smaller than 350 ns (i.e. 3–4 bunch crossings), thus allowing the use of the FTDs for triggering,

– to cope with the problem of track finding in dense forward jets, and

– to reduce the effect of the strong and rather inhomogeneous magnetic field present in the FTD region on the calibration of the chambers.

Five field shaping strips on either side of the drift cell (2 mm wide and spaced by 2 mm) allow to produce a homogeneous electric drift field even at the edges. All planar electrodes, i.e. cathodes, field strips, and outer shielding, were made by printing and etching the Cu cladded boards.

The potentials of the wires, cathodes, and field shaping strips were optimized in view of the following criteria:

– Minimal inhomogeneities of the drift field at the edges of the cell.

– Equal surface fields (gas gain) on all six sense wires.

– Surface field on potential wires below 20 kV/cm (to avoid whisker growth).

Table 2
FTD (RTD) cell parameters

Inner cell dimensions	24×48 mm^2
Number of sense wires/cell	6
Number of potential wires/cell	7
Number of field strips/cell	10
Material of sense wire	W + 3% Re, gold plated
Diameter of sense wire	30 μm
Material of potential wire	Mo, gold plated
Diameter of potential wire	121 μm
Voltages	
Sense wire	1860 V
Potential wire	0 V
Field strip S1-5	−550 V
Field strip S2-4	−50 V
Field strip S3	630 V
Cathodes	−1140 V
Drift field	≈ 1.25 kV/cm
Gas mixture	Ar/ethane (50/50) + ethanol
Gas pressure	atmospheric
Drift velocity	52 μm/ns
Max. drift time at max. B	350 ns
Gas gain	$\approx 5 \times 10^4$

– Minimal electron drift to potential wires or field strips.

– Electrostatic deflections are small compared to the gravitational sagging of the sense wires.

The initial optimization was done with the help of the programs WIRCHA [1] and DRIFT [2] and fine tuned experimentally. The resulting set of potentials for a gas mixture of argon/ethane (50/50) at atmospheric pressure is shown in Table 2. The corresponding drift field is about 1.25 kV/cm and the gas gain is about 5×10^4.

The cathodes and field strips are electrically subdivided, such that the gas gain can be reduced in the region around the beam pipe in case of intolerably high backgrounds from beam gas interactions or synchrotron radiation.

3. Mechanical construction

In this paper we present a brief description of the chamber construction. Details can be found in refs. [3,4].

3.1. Chamber body

As shown in Figs. 2 and 3, each chamber layer is composed of two vertical disklike walls and smaller cathode walls between them forming long rectangular cells.

All the walls were made of glass fiber epoxy boards (EGS 619/FR4), 1 mm thick, with a copper cladding of 18 μm on either side. The construction of the chamber body was done as follows: The indentation slots and holes for the bearings of the wire supports were punched by a computer controlled machine. The cathodes, the field shaping strips, and the outer shielding pattern was silk printed on the boards. The copper was etched using a solution of $FeCl_3$. After cleaning of the surfaces and HV tests the walls were glued together with Araldite using an indentation technique, thus forming a multi-I-beam structure. To seal the remaining leaks in the indentation slots thin sheets (0.2 mm) of FR4 were glued onto either side of the layer.

Three such layers were glued together with another 0.2 mm glass fiber exopy sheet (for insulation) in between and with the cells of neighboring layers at ±120° w.r.t. each other. In this way the mechanical structure of the chamber body becomes similar to a honeycomb structure. It was completed by gluing two more 0.2 mm sheets onto the outer disks.

The internal support structures at the outer rim (Figs. 2 and 4) as well as at the beam pipe hole were mounted only after the wiring of the chamber, the adjustment of the combs, the installation of the internal cabling (signal, HV) and various tests of the circuitry.

3.2. Wire stringing

The material and diameter of the wires are described in Table 2. The potential wires were strung with 5 N, resulting in a maximum gravitational deflection of 120 μm for the longest wires. The sense wires were strung with 0.6 N, which equalizes the amount of sagging for both types of wires. The wire tensions are well below the limit of proportionality. The choice of molybdenum and tungsten was motivated by the similarity of their linear coefficients for thermal expansion.

The wires were mounted as illustrated in Fig. 3 by using moulded combs made out of ULTEM. The wire position is defined by precision grooves in the combs. At the outer end the wires were fixed mechanically by small brass cones squeezed into brass feedthroughs and by soldering.

Wiring a cell was done according to the following steps:

– All 13 wires of a cell were strung and fixed to both combs on a wiring bench which allowed for a precise adjustment of the required distance between them. The desired wire tension was produced by attaching a proper weight to the loose end and squeezing the wire at the second mount. It was checked by measuring the mechanical resonance frequency.

– A Kapton foil was soldered to the feedthroughs on the readout end. This foil provides flexible leads for the signals and the HV, and it supports protective resistors as well as coupling capacitors.

– A slim tool which allowed for a precise adjustment of the length was attached to the two wire mounts.

– This assembly was slid into the cell and was adjusted such that the mount at the far end was aligned with respect to the bush bearings in the walls. The springs were released and the eccentric cylinders engaged the bearings.

– After checking the wire tensions, HV tests of the sense and the potential wires were performed.

3.3. Precision of wire location

The influence of all relevant alignment errors on the reconstruction of three-dimensional track elements (as measured by one chamber) was studied by Monte Carlo calculations. In view of a target value for the spatial resolution of $\sigma = 100$ μm the following tolerances are required:

– Internal accuracy of the combs (depths and spacing of grooves) ± 30 μm

– $u(v, w)$-position of the combs (for the coordinate system see Fig. 3) ± 30 μm

– Zeroes of the $u(v, w)$-scales ± 20 μm

– z-position of the combs of all three layers ± 100 μm

– Angles between wire directions of adjacent layers ± 0.5 mrad

(Note, we quote here and throughout this section tolerances rather than rms values.).

The internal geometry of the combs, i.e. the depth of the grooves and their spacing in z, was measured to be accurate within ± 25 μm. This means that the errors of the wire locations in the chamber is dominated by the errors of the comb locations. The reference marks of all combs were therefore viewed by means of a levelling instrument. The comb axes were aligned to be horizontal by turning the eccentric cylinder fittings. The tilt angles were adjusted and the position was rechecked. An accuracy of ± 40 μm was achieved. The accuracy of the angles between the wire directions of adjacent layers was given by the accuracy of the punched dowel holes and their distance from the symmetry axis of the chamber structure. It was better than ± 0.2 mrad.

The accuracies achieved by optical survey methods cannot fully meet the requirements quoted above. This is particularly true for the zeroes of the u (v, w) scales as well as for the relative positions and orientations of the tracking chambers in ZEUS. Straight and isolated tracks will have to be studied to improve our knowledge.

If the temperature in the running ZEUS detector will differ significantly from room temperature thermal expansion will alter the wire positions. For two cells separated by 2 m, e.g. in FTD3, the thermal shift is 15 μm per degree. Again the analysis of straight particle tracks can yield the information. The same is true for the effects of gravitational sagging, which is 120 μm at maximum.

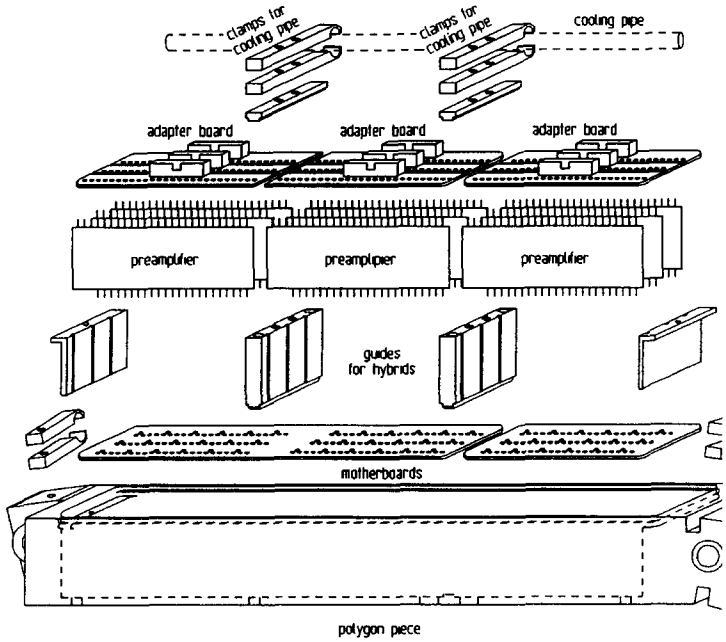

Fig. 4. Mounting of on-chamber ancillaries on the aluminium support structure.

3.4. Internal cabling

Inside each layer the HV is distributed by means of custom made daisy chains which were manufactured ahead of the installation. All loose ends of the chain, except the one for the HV connector, are equipped with 1 MΩ protective resistors.

The internal signal cables from the coupling capacitors to the preamplifier motherboards were soldered to the capacitors already during the manufacture of the Kapton foil assemblies.

3.5. Internal support structures

To reinforce the chamber body a light-weight aluminium structure was introduced into the outer rim of each layer. The structure is composed of twelve pieces per layer forming a polygon. The 36 aluminium pieces were installed after the completion of the internal cabling. This rim structure supports the weight of the chamber and takes all external forces. The cutouts in the polygon pieces are used to accommodate the preamplifier hybrids thus providing good electromagnetic screening, see Fig. 4. Water pipes were bolted on the aluminium pieces to provide cooled surfaces surrounding the electronics.

The reinforcement structure at the inner (beam pipe) hole is comparatively thin and simple. It is composed of rings and spacers made of glass fiber epoxy, which were bolted and glued to the chamber walls. The structure supports the inner gas enclosure consisting of an aluminium cylinder of 0.5 mm thickness.

3.6. Chamber sealing

The little space available and the thin structural elements which would not stand the necessary local pressure did not permit the use of O-rings. The gas volume was therefore sealed throughout by gluing.

The cracks at the inner hole and between the boards and the outer aluminium pieces as well as the bolt heads were sealed with Scotch-Weld 2216 B/A, an elastic two-component glue. The elasticity is required to avoid fissures in the glue due to tiny stresses or shears which cannot be avoided completely while handling the chamber. Sealing the preamplifier boards and the aluminium sheets inside the polygon pieces was done with silicone rubber to facilitate reopening single cutouts for inspection or repair.

It was demonstrated by experimental checks that the gas seal can stand safely an internal overpressure of 30 mbar. The maximum overpressure for emergency flushing is 10 mbar while the normal operation requires only 2 mbar.

3.7. Chamber tests

Before soldering the signal leads to the motherboards and before sealing the motherboards each chamber was flushed with N_2 or CO_2 and HV tested. The outer ends of the signal leads were grounded to have the full voltage across the coupling capacitors. The sense wire voltage was typically raised to 2.3 kV.

After the completion of the chamber sealing each chamber was flushed with a multiplying gas mixture $Ar/CO_2/C_2H_6$ (88/10/2) or Ar/C_2H_6 (50/50). Attempts to raise all voltages to their nominal values and polarities revealed in a few cases problems, which were cured after temporarily removing single motherboards. Then the preamplifiers were mounted and all readout channels were tested with a radioactive source and an oscilloscope.

After installation of the complete forward tracking detector into the ZEUS detector, the leak rates were again measured by pressurizing the chamber and observing the pressure decrease with time. All readout channels were tested by feeding test pulses into the preamplifiers and measuring the output. In addition the HV was turned on after flushing all chambers with $Ar/CO_2/C_2H_6$ (88/10/2) and single rates of all wires were taken. Only a small number of channels ($< 1\%$) was found not to work.

4. Gas system

The gas system for the FTDs/RTD is a simple open flow system without recirculation with three independent gas lines. The components are mixed in the gas house using regulators controlled by mass flowmeters. This mixture is bubbled through temperature controlled ethanol. Two summary gas flowmeters in the gas house (up- and downstream of the chambers) check for leaks in the system. Individual combinations of flowmeters and mechanical regulators in the experimental hall distribute the gas among the four chambers according to their different volumes. The gas leaving the chambers is pumped back to the gas house and exhausted over the roof of the gas house. During the commissioning of the detector a nonflammable gas mixture of $Ar/CO_2/C_2H_6$ (88/10/2) was used instead of the nominal Ar/C_2H_6 (50/50) mixture.

5. High voltage system

The six different potentials needed for each drift cell (sense wires, potential wires, cathodes, and three types of field shaping strips) are supplied via individual cables from the HV electronics in the electronics hut. No resistor chains are used. This allows measuring the

individual chamber currents directly and in an unbiased way and it avoids additional power dissipation inside or close to the chambers. Additional HV channels are used for supplying the cathodes and field strips of all cells close to the beam, which are subdivided in order to reduce the gas gain in case of high backgrounds. In total there are 40 HV channels, connected to one CAEN SY127 HV crate [5].

In order to prevent excessive currents in the chambers the distribution system is equipped with two types of switches for each channel. A passive diode circuit increases the effective internal resistance of the HV channel to 100 MΩ, resulting in a fast breakdown of the HV. An additional read relay interrupts the line when 10 μA are reached. This relay can also be opened by hand if a local problem occurs while the other cells can still be operated. It has the important feature that the HV remains constant even if the chamber currents change due to varying background conditions.

6. Analog electronics

Signal amplification is done in two stages, by preamplifiers mounted on the chamber and by post-amplifiers in the electronics hut with adjustable gain to match the signal amplitude to the dynamic range of the flash-ADCs. The analog electronics was designed and built by the University of Siegen [6].

6.1. Preamplifiers

Signals from the sense wires are fed into the preamplifiers via 470 pF capacitors on the Kapton foils. The charge sensitive preamplifier is mounted on a motherboard inside the outer aluminium support structure (Fig. 4). It is a low power SMD hybrid (2.3×6.8 cm^2) with six channels corresponding to the six sense wires of a cell dissipating about 1 W. The amplifier has a conversion factor of 1 mV/$5000e_0$ and an equivalent noise charge of about $3500e_0$. The signal rise time is about 4 ns, corresponding to a bandwidth of 90 MHz. Each hybrid is equipped with a test signal input, which is capacitively coupled to all six input channels. The output provides a bipolar signal connected to the postamplifier by a 50 m long twisted pair cable [7].

6.2. Post-amplifiers

The post-amplifier – a two-channel hybrid – consists of three parts: a differential amplifier with adjustable gain, a pulse shaping pole-zero filter and another amplifier. The difference of the bipolar input signal is amplified by the first amplifier stage and fed into the pole-zero filter. This filter is used to shorten the falling edge of the pulse to reduce pileup effects. The gain and pulse shaping of each hybrid was carefully adjusted to ensure equal response of all channels [8].

7. Digital electronics

Due to the short HERA bunch crossing interval of 96 ns the sampling frequency of the FADCs is 104 MHz. For the same reason the processing of the FADC outputs called for a special development of the various modules. To keep the readout electronics for all chambers of the inner tracking system as uniform as possible only the FADC modules are different for the planar chambers (FTDs and RTD) and for the central tracking device (CTD). The latter FADC modules as well as all components of the environmental electronics were

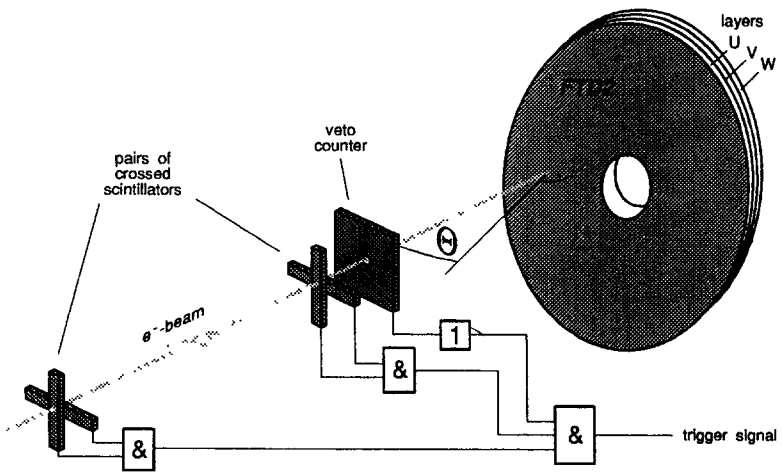

Fig. 5. FTD2 test beam setup.

designed and built by the Rutherford Appleton Laboratory and partly by the other British ZEUS groups [9], while the FADC modules for the FTDs/RTD are a design of the University of Siegen [10].

In a Siegen-type module the FADC data can be pipelined for a maximum of 40 μs (hardware limit). On a positive first level trigger signal (FLT) which has to appear within a maximum of 5 μs (FLT limit) a selectable block of data is transferred to a primary event buffer. While copying the data to a secondary event buffer they are processed by a digital filter of the FIR type, providing an effective data reduction at the earliest possible stage and thus a minimum dead time of the front-end electronics.

The contents of the secondary event buffers of all FADC modules in a crate are collected by a readout controller which is part of a transputer network. The same network performs the extraction of the drift time and the dE/dx information and stores the results until the arrival of a second level trigger signal. After a positive decision the data of an event are passed to the ZEUS event builder.

8. Test beam results

Before the installation of the FTDs in ZEUS the second largest chamber (FTD2) was tested at DESY with electron beams of energies between 0.5 and 3 GeV. Efficiency, tracking and dE/dx were investigated.

8.1. Test beam setup and data taken

Fig. 5 shows a schematics of the setup. Before hitting the chamber, the electron beam had to traverse a 1 cm^2 squared collimator and two pairs of finger counters which were read out by four photomultipliers and were used to trigger the data acquisition system. A scintillator paddle with a 1 cm^2 squared hole in the middle served as a veto.

The FTD2 was placed such that the wires in the w plane were always vertical. Only 12 (4 per plane) of the 264 cells of the chamber were instrumented.

The gas mixture used was Ar/C_2H_6 (50/50). The analog electronics were of the final design. All the postamplifier gains were set to give similar output pulse heights for the same input signal at the preamplifiers.

Since the final readout electronics (section 7) was not yet available, the readout was performed by a 6 bit STRUCK DL301 FADC system [11] with a sampling frequency of 100 MHz and a nonlinear response function to expand the dynamic range to effectively 8 bits. We will refer to an FADC pulse as the one obtained after correcting the FADC contents for the nonlinear response function.

Runs of approximately 10000 events each were taken at different conditions:

1) Incidence angle (angle formed by beam and chamber axis) of 0°, 15°, 20° and 30°. The beam energy was 2 GeV. Notice that the maximum incidence angle of the particles coming from the interaction region in ZEUS is approximately 30°.

2) The beam incidence position on the detector was changed by moving the chamber vertically and horizontally in the plane perpendicular to the beam (steps of 5 mm). The incidence angle was 15°.

3) Beam energies of 0.5, 1, 2 and 3 GeV. The incidence angle was 15°.

8.1.1. Signal processing

The relevant information provided by the digitized signals was extracted alternatively using three different types of signals:

– The original digitized signal.

– The difference of samples pulse (DOS) as proposed in ref. [12]. The relation between the original contents $x(iT)$ (where $T = 10$ ns is the bin width of the FADC and i runs from 1 to 100) and the DOS signal output $z(iT)$ reads

$$z(iT) = x(iT) - x((i-1)T).$$

This operation corresponds approximately to a differentiation of the original pulse shape.

– The output pulse from an infinite impulse response (IIR) digital filter applied to the original FADC signal as proposed in ref. [13]. The relation between the original and the IIR-filtered signal output $y(kT)$ is (see for example ref. [14])

$$y(iT) = \sum_{j=0}^{m} D_j x(iT - jT) + \sum_{j=0}^{m} C_j y(iT - jT),$$

where m, D_j and C_j are constants characterizing the filter. They were set to a bandpass filter with a frequency of 20 MHz and a Q-value of 1 (Q is the ratio of frequency and bandwidth) [13].

Fig. 6 shows a typical FADC output signal (a) and the corresponding DOS and IIR-filtered pulses (b and c respectively).

8.2. Results on tracking

For hit identification, a number of successive DOS bins above a threshold with the integral sum of their contents exceeding some chosen value was requested (for details see ref. [15]). The drift time was calculated as the weighted mean of the positive part of the DOS pulse, see Fig. 6. The drift times were converted into drift distances using a computed space drift time rela-

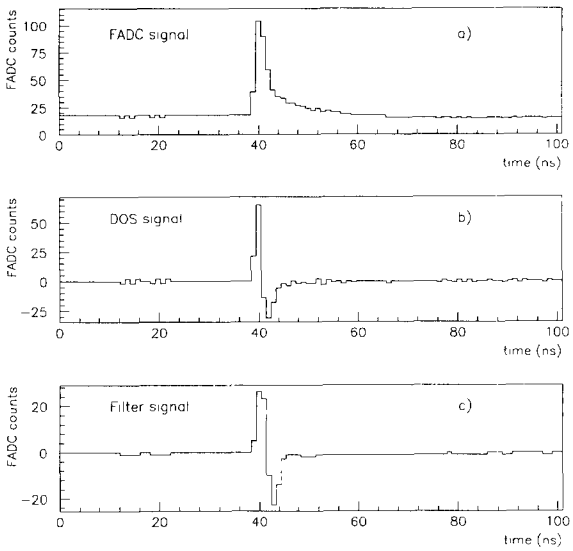

Fig. 6. A typical FADC pulse (a) and its corresponding DOS and IIR-filtered pulses (b) and (c).

tion [16] based on the measurements and electric field calculations from ref. [17].

An identified signal on a wire was used for the analysis only if:

1) there was only one hit per event identified,

2) the estimated drift time after subtraction of the contribution from cables, readout electronics etc. (t_0 correction) was smaller than 280 ns,

3) the FADC signal did not contain any overflow per bin, i.e. the pulse height did not exceed 200 mV.

8.2.1. Reconstruction of track projections

The projections of the particle track were reconstructed cell by cell by fitting the space points corresponding to the calculated drift distances to a straight line. To solve the left–right ambiguity all possible combinations of the space points (above and below the wire plane) were taken into account. The line resulting from the combination which gave the smallest variance in the fit was chosen as the true track.

For a track projection to be considered valid, a minimum of 5 hits and a variance per degree of freedom smaller than 20 were required. Notice that in our fitting procedure, a variance of 20 corresponds to a mean distance of 400 μm from the reconstructed points to the fitted track.

The distributions of the track residuals, $y_{\text{fit}} - y_{\text{measured}}$ (the coordinate system inside a cell is shown in Fig. 12), were found to be Gaussians with very similar parameters for all channels investigated. The standard deviations of Gaussian fits to these distributions (σ^{meas}) are related to the spatial resolution of each wire by $\sigma_t = \sigma_t^{\text{meas}}/\alpha_t$. The factors α_t take care of the bias introduced into the track fits by the small number of wires contributing to them. They range from 0.9 to 0.7.

Fig. 7 shows as an example the single wire resolution, averaged over the six wires in a cell, as a function of the distance from the track to the wire, for two cells. For drift distances larger than 3.5 mm an almost constant value of about 105 μm is observed. When the track approaches the wire, the resolution deteriorates. This is partly expected from the distribution of ionization clusters along the track. The fact that the deterioration starts already at distances of a few mm indicates, however, that the space drift time relation needs fine tuning. This will be done with data taken in ZEUS to include simultaneously the effect of the magnetic field.

Already at cell level the left–right ambiguity was resolved correctly for about 96% of all reconstructed projections. This is demonstrated by Fig. 8 which shows the reconstructed polar angle for a cell of layer w. Because of the particular geometry of the setup, the reconstructed polar angle should coincide with the angle of incidence of the beam. The approximately 4% of wrongly reconstructed slopes appear at −300 mrad. Most of them can be recovered using the track information of the other two layers.

When the particle trajectory crosses two adjacent cells of the same layer, the reconstruction is performed using the information from both cells. This implies the introduction of the relative positions and angles between both cells, which were determined by optical surveying of the detector. Their uncertainties contribute to the fit variance, which is slightly shifted to larger values. But nevertheless the single wire resolution is still close to 105 μm.

8.2.2. Efficiency

The tracking efficiency of each wire was determined by requiring a track reconstructed from the hits on the remaining 5 wires of the same cell, again applying a

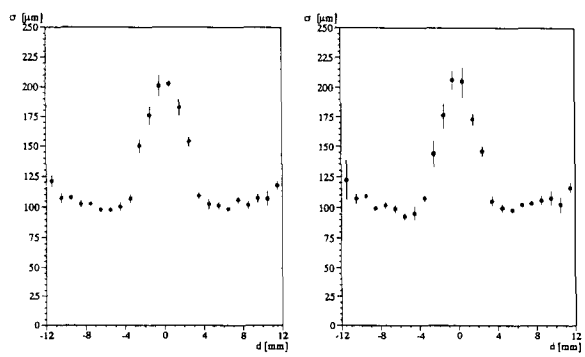

Fig. 7. Wire resolution, averaged over the six wires in a cell, as a function of the drift distance. The two figures correspond to two different cells.

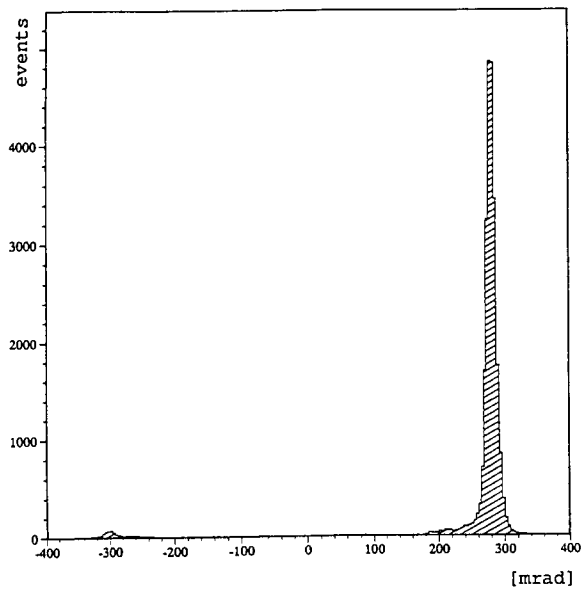

Fig. 8. Polar angle reconstructed in one of the cells in the w plane.

variance cut at $\chi^2 = 20$ (section 8.2.1), and by comparing this prediction with the response of that wire. In about 3% of all tracks the prediction was outside the cell. For geometrical reasons this was possible only for the outermost wires (1 and 6). These events as well as overflow hits (2.5%) and double hits (3.7%), which can in principle be used in the analysis, were included in the calculation of the efficiency. With these definitions the efficiency was found to be 99.7% for the inner wires (2 to 5) and 99.1% for the wires 1 and 6, resulting in an average efficiency of 99.5%.

8.2.3. Three-dimensional track reconstruction

To study the reconstruction of the particle trajectories in space, a global coordinate system was established. The y axis is defined perpendicular to the wire planes for cells in layer v, while the x axis is parallel to the wires of these cells, and z points to the same hemisphere as the beam. In this frame a track in space can be specified by

$$x(z) = x(z_0) + a_x z, \qquad y(z) = y(z_0) + a_y z,$$

where z_0 is an arbitrary value of the z coordinate, chosen to be in the middle of layer v, i.e. the center of the chamber.

Each FTD chamber measures three projections of the particle trajectory. Calling $u(z)$, $v(z)$, $w(z)$ the y coordinate of the cell reference system (see Fig. 12), for layer u, v and w respectively, the three projections can be written as

$$u(z) = u(z_0) + a_u z,\ v(z) = v(z_0) + a_v z,$$
$$w(z) = w(z_0) + a_w z.$$

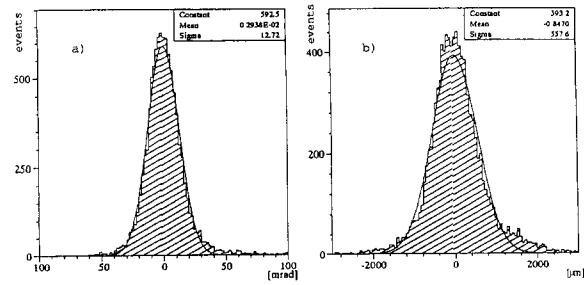

Fig. 9. Measured sum of slopes (a) and sum of free parameters (b) for tracks with the three projections reconstructed. The incidence angle was 15°.

Because of the geometry of the FTD chambers, the following relations exist:

$$u(z_0) + v(z_0) + w(z_0) = 0,\ a_u + a_v + a_w = 0.$$

Fig. 9a shows the sum of measured slopes of the three track projections from a run with a 15° angle between the beam and the z axis of the chamber (i.e. the beam incidence angle). The expected relation holds well. The width of the distribution is a measure of the angular resolution of the cell $\sigma_{\text{cell}} = \sigma_{\text{sum}}/\sqrt{3} = 7.3$ mrad. Fig. 9b shows the corresponding distribution for the sum of the free parameters of the reconstructed projections. Also in this case the expected behavior is observed. The relatively large width is due to the necessary extrapolations to z_0 which involve additional error propagations. The z distances have yet to be precisely measured with tracks.

From the measured values $u(z_0)$, $v(z_0)$, $w(z_0)$ and a_u, a_v, a_w one can extract $x(z_0)$, $y(z_0)$ and a_x, a_y. Only two projections are necessary to reconstruct the particle trajectory in space. The third one provides a useful redundancy.

In this paper, the resolution for the reconstruction of the position and of the angle is defined as the value at which the integral over the corresponding error distribution reaches 66% of the total. Table 3 shows the values obtained for the resolutions of x, y, a_x, a_y in the coordinate system under consideration and in the one in which the resulting errors become equal (rotated by 45° around the z axis).

Table 3
Resolution of position and angle for two different global coordinate systems

Coordinate system	y parallel to wires at v	y 45° to wires at v
σ_x [μm]	116.1	88.5
σ_y [μm]	49.4	88.4
σ_{α_x} [mrad]	1.02	2.68
σ_{α_y} [mrad]	3.66	2.66

ne chamber concerning dE/dx
so investigated. Details are de-
Only low energy electron beams
were available and therefore no
d be attempted of the signals pro-
ent particle types. The study concen-
behavior of the charge collected on the
arying the beam energy, the amount of gas
by the particles and the relative direction
the beam and the wires. Regular and IIR
filtered signals were used for this analysis.

8.3. Results on

8.3.1. Data analysis

Two corrections, cross talk and calibration, were applied to the digitized signals for all events before any further processing. The signals were then passed through the digital filtering process and the energy loss was calculated.

Cross talk: The correction for cross talk was done event by event and channel to channel by adding to the signal of a given wire the signals of the neighboring wires, weighted by a correction factor (the sum was done bin by bin). The correction factor of 10% was obtained from a study of the cross talk using a radioactive source [4].

Calibration: To further equalize the response of the readout channels, correction factors were applied bin by bin to all FADC output streams. For the majority of the wires these correction factors were estimated by comparing the most probable values of the charge distributions with 0° data. Only pulses away from the wire (4.5 to 10 mm drift distance) and corrected for the staggering effect (see next section) were included in the distributions. The normalization was done to the mean of the uncorrected most probable values. In the case of wires for which we had no data at 0° the comparison was done at 15°, taking as reference already corrected signals. Typical deviations ranged over 10% and the maximum observed was 50%.

The signal pedestal was estimated by averaging the contents of the first 10 FADC bins after the two corrections above were applied.

The charge collected on the wire was obtained in two different ways: a) by integrating the FADC pulse over the first 20 samples (200 ns) after the start of the pulse, the result being referred to as "total charge", and b) by integrating the positive part of the filtered signal (see Fig. 6), called "filtered charge". Wires with more than one reconstructed pulse per event were not used in the analysis.

Fig. 10 shows a typical distribution for the charge collected on a wire after correction for the distance travelled by the particle inside the active volume of the wire (a) total charge, b) filtered charge). The energy

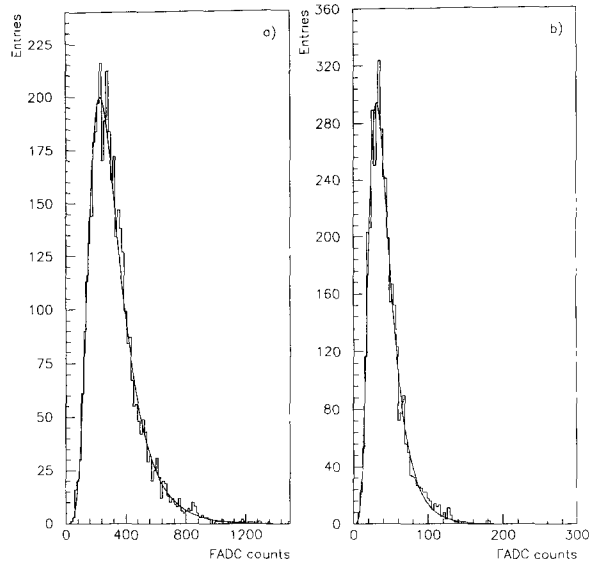

Fig. 10 Typical distributions of the charge collected at one wire using regular pulses (a) and filtered signals (b). The curves show the fits to a Moyal function.

and incidence angle of the electron beam was 2 GeV and 15°, respectively. The curves on top correspond to fits using a Moyal function [19]. Both total and filtered charge distributions have the expected Landau-type structure with a FWHM of approximately 110%.

8.3.2. Systematic corrections

To obtain a measure for the specific energy loss, the measured values were corrected for differences in the charge collection due to the staggering of the wires, electronic capture (attachment) and saturation. The corrections were done pulsewise. A description of these effects and a method to correct for them is given in ref. [20].

The correction factors were estimated by studying the behavior of the most probable value of the distributions for the charge collected per wire, when varying the beam energy and the relative angle between wires and beam. The most probable values were obtained from a fitted Moyal function. To minimize the effects of the long Landau tail, only those bins with a content larger than half the maximum were used in the fits.

Staggering: The staggering of the sense wires leads to a slight difference in the charge Q collected on the wires staggered towards the track (near) or away from the track (far). To estimate quantitatively this effect, the ratio $Q_{\text{far}}/Q_{\text{near}}$ was measured for those wires which had collected enough pulses both *near* and *far*. In order to minimize the contribution from other effects only particles at 0° and at least 3 mm away from the wire were used. We obtained $Q_{\text{far}}/Q_{\text{near}} = 1.07$ and a dispersion of 0.01. The signals were normalized to that left by a *near* particle.

Attachment: Fig. 11 shows the dependence of the most probable value of the charge collected as a function of the drift distance for the six wires of a cell. In order to minimize the contribution of other effects, only particles at 0° and at least 3 mm away from the wire were used. In addition, for each wire the distribution contained only pulses either *near* or *far*. At the outermost wires of the cell (1 and 6) the measured charge decreases with drift distance, whereas it increases at the inner wires (2 to 5). Similar results were obtained with the other cells.

A likely explanation of the observed behavior is the following. Because of the high gas gain at which the chamber was operated and the small drift distances involved, appreciable saturation (see next section). They should be tant as drift distances get smaller a proaches perpendicularity to the wire (s refs. [21] and [20]). Fig. 11 shows that the dependence on the drift distance is nonnegl the FTDs, and dominates over attachment at the wires. The higher attachment at the outermost w could be explained by their closeness to the chambe walls. The HV settings for the field shaping strips are not yet fine tuned, and non optimal values could translate into a smaller density of field lines at those wires, reducing therefore saturation.

To correct for these effects the signals were normal-

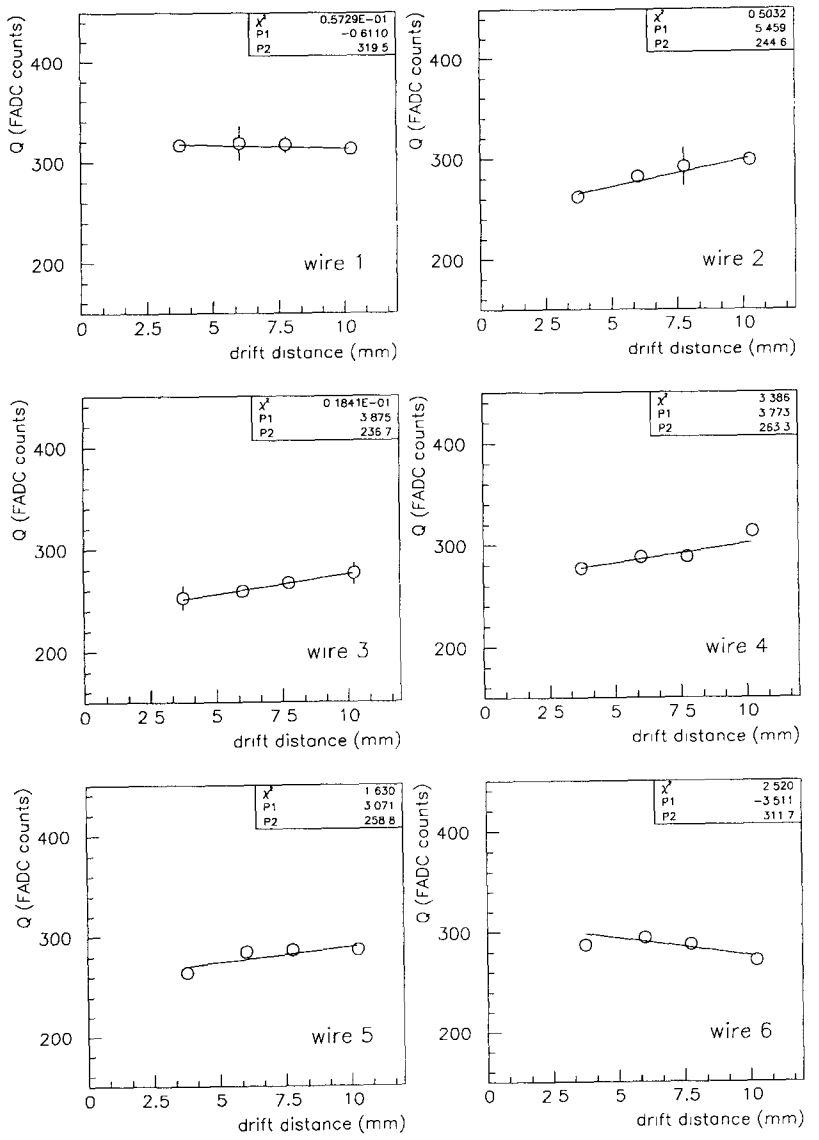

Fig. 11. Charge collected as a function of the drift distance for the six wires of a typical cell.

ized to that left by a particle passing 3.75 mm away from the wire assuming a linear dependence on the drift distance

$$Q = Q_{\text{measured}}/1 + A(d - 3.75),$$

where d is the drift distance in mm and A was obtained by averaging the measured dependence for the inner and outer wires: $A_{\text{inner}} = 0.016 \pm 0.003$, $A_{\text{outer}} = -0.007 \pm 0.006$.

Saturation: The presence of saturation causes a rather complex dependence of the energy loss measurement on the track parameters of each particle, i.e. on its primary ionization density, its drift distance and its track orientation. The dependence of the charge collection on the drift distance was studied in the previous section. Here the dependence on the track orientation is investigated. No attempt was made to study the effect on the primary ionization density.

In the cell reference frame, the particle track orientation is specified by the two angles ϕ and θ formed by its projections on the zx and zy planes and the z axis respectively (see Fig. 12).

When the track angle θ is larger than 0° there is a slight difference in the time of arrival at the amplification region of the primary ionization electrons created along the track segment (see Fig. 12) and therefore the expected reduction of the electric field for later electrons will be smaller. If the track angle ϕ is larger than 0° the arrival of the primary ionization electrons to the amplification region is not-anymore concentrated in a single space point on the wire but spread out, also reducing saturation.

Fig. 13a shows the θ dependence of the charge collected for wires of layer w. The points represent the mean of the most probable values obtained for the different wires and the error bars show their dispersion. Because of our setup, the corresponding ϕ angles are always very close to 0° (see Fig. 12) and therefore

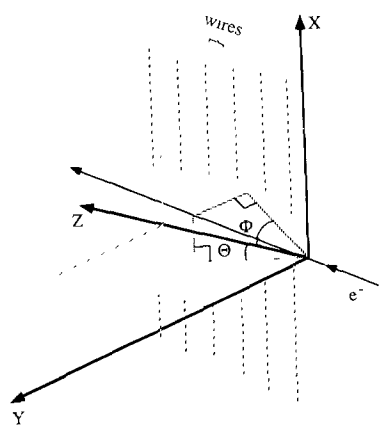

Fig. 12. Cell reference frame and track angles used to parametrize systematic effects on dE/dx.

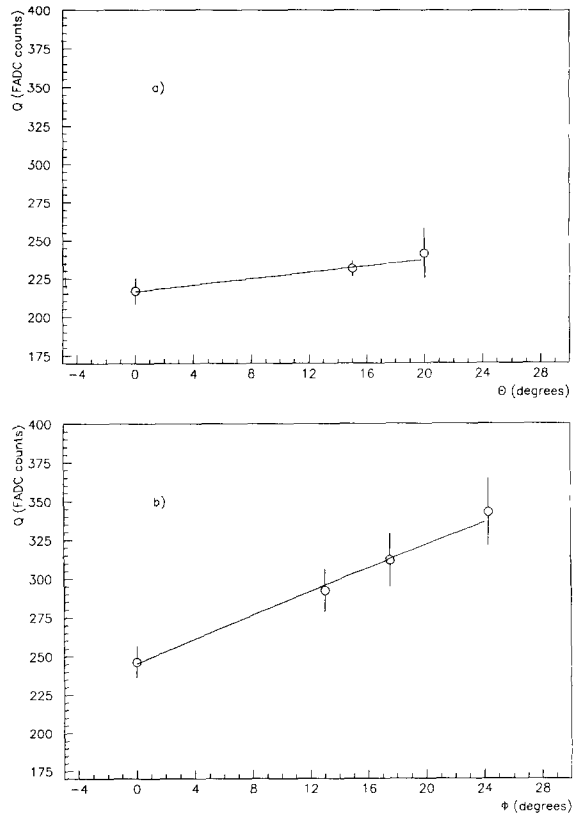

Fig. 13. Charge collected as a function of the track angle θ for wires in layer w (a) and as a function of ϕ for wires in layers u and v (b).

the mild dependence observed is expected to come from the differences in the time of arrival to the wire of the ionization electrons discussed above. Fig. 13b shows the ϕ dependence of the charge collected for wires of layers u and v. The stronger dependence observed here is therefore expected to come mainly from the spreading out of the avalanche along the wire.

The θ and ϕ dependence of the charge collected were parametrized by

$$Q_{\text{measured}} = Q(1 + A_\theta \sin\theta),$$

$$Q_{\text{measured}} = Q(1 + A_\phi \sin\phi).$$

From fits to the data (solid lines in Fig. 13) the values $A_\theta = 0.28 \pm 0.18$ and $A_\phi = 0.91 \pm 0.22$ were obtained. To correct for this effect of saturation, the signals were normalized to that left by a particle crossing the cell at $\theta = \phi = 0°$.

8.3.3. Results

In one chamber, the energy loss of a particle is sampled 18 times along its track. To reduce the effect of the long Landau tail in the determination of the mean energy loss per particle, a "truncated mean" was

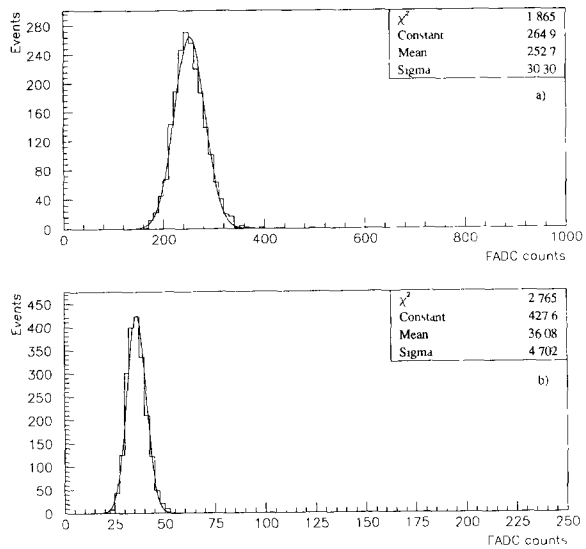

Fig. 14. Truncated mean distribution for 2 GeV electrons under an incidence angle of 15° obtained with total charge (a) and filtered charge (b) pulses. The lines are fitted Gaussian distributions.

calculated, where the samples with the largest energy loss were not used. Only events with at least 15 recognized pulses with drift times larger than 50 ns and with a reconstructed particle track were considered for the following analysis.

The amount of truncation for an optimum particle separation was estimated to be about 30% [20]. We eliminated in this analysis only 17–20% of the samples (3 out of 15–18) because of the low number of reconstructed pulses per event that we had under certain conditions (resulting from the limited number of readout channels).

Fig. 14 shows the truncated mean distribution for 2 GeV electrons under an incidence angle of 15° obtained with total charge (a) and filtered charge (b) pulses. The curves are fitted Gaussian distributions.

We define the dE/dx resolution of an FTD chamber ($\Delta(dE/dx)$) as the standard deviation of the distribution fitted to the measured truncated mean values.

The truncated mean follows an approximate Gaussian distribution with a σ that depends both on the Landau distribution for the energy deposition (which at the same time depends on the characteristics of the chamber) and the number of samples used in its calculation. This σ will be taken as the intrinsic component of $\Delta(dE/dx)$ and will be called σ_{intr}. To estimate it Gaussians were fitted to the truncated mean distributions obtained for the different conditions under study (different beam energy, different incidence angles) obtaining very similar σ's (within 10%). σ_{intr} was taken as the mean of all of them. After including a factor $1/\sqrt{3}$ to take into account the other two chambers in the forward detector, the results were (statistical errors are negligible): $\sigma_{intr}^{tot} = 6.5\%$ using the total charge and $\sigma_{intr}^{fil} = 7.6\%$ using the filtered pulse.

Notice the wider distribution obtained if filtered pulses are used. A tuning of the digital filter parameters may improve this result.

The second contribution to $\Delta(dE/dx)$ comes from our limited knowledge of the processes that occur when the particle crosses the chamber and in particular from uncertainties in the correction factors applied to the data. As they will translate into systematic deviations of the measured dE/dx from the real values, we call this contribution σ_{syst}. The value taken for σ_{syst} for the FTD2 is the rms of the distribution formed by:

1) The observed deviations of the mean values of the truncated mean distributions, with respect to expectations, when varying the beam energy (Bethe–Bloch prediction) and incidence angle (constant behavior).

2) The deviations from the constant value when varying the incidence position of the beam (vertical and horizontal chamber displacement).

The results were $\sigma_{syst}^{tot} = \sigma_{syst}^{fil} = 6.0\%$, with a statistical error of $\pm 1.2\%$. Unlike the intrinsic resolution σ_{intr}, the contribution σ_{syst} obtained for the FTD2 cannot be extrapolated in a simple way to an expected σ_{syst} for the three-chamber setup. We therefore estimate an upper limit for $\Delta(dE/dx)$ by adding in quadrature σ_{syst} (FTD2) to σ_{intr} (three chambers) which gives

$$\Delta(dE/dx)^{tot} < 8.8\%, \quad \Delta(dE/dx)^{fil} < 9.7\%.$$

With this resolution a reasonable electron–hadron separation for low energy particles (0.5 to 5 GeV) can be achieved, in particular in combination with the other methods of electron identification provided by the ZEUS detector.

9. Conclusions

The design and construction of the ZEUS forward tracking detector has been described. Test beam measurements performed at DESY confirm the design specifications, namely 99.5% efficiency, 105 μm single wire spatial resolution, 90 μm and 2.7 mrad for three-dimensional track coordinates and slopes, respectively, and an upper limit of the dE/dx resolution of 8.8%.

The detector was installed into the ZEUS detector in November 1991. Test data were taken in 1992 and 1993 with only a limited amount of readout electronics. The final FADC electronics is expected in early 1994.

Acknowledgements

During the design and construction phase as well as when the chambers were installed in ZEUS we received most valuable technical help from W. Ockenfels, A. Nachtsheim, B. Neff, A. Sellmann, F. Czempik, and E. Weiß. We are very grateful to them. In addition we would like to thank F. Gallardo, A. Varela and P. Varela for their help during the wiring and testing of the chambers in Madrid. We also thank M. Hauschild for his help in understanding the saturation effects.

We are indebted to DESY for providing the infrastructure and technical support during the completion of the chambers on site and during the beam tests. One of us (F. Barreiro) would like to thank the Alexander von Humboldt Stiftung for supporting his stays at Bonn and DESY. L. Labarga would like to acknowledge support from CAM, Madrid, during his stay at DESY while the test beam measurements and final assembly of the detector were being done.

References

[1] J. Fehlmann et al., WIRCHA program, ETH Zurich (1984).
[2] J. Va'vra and L. Roberts, DRIFT program, SLAC (1982).
[3] B. Gutjahr, Doctoral Thesis, BONN-IR-93-17, Bonn University (1993).
[4] S. Kramarczyk, Doctoral Thesis, BONN-IR-93-45, Bonn University (1993).
[5] Construzioni Apparecchiature Elettroniche Nucleari S.p.A., 55049 Viareggio, Italy.
[6] E. Badura et al., Nucl. Phys. B 23A (1991) 239.
[7] J. Meyer, Diploma Thesis, BONN-IR-90-09, Bonn University (1990).
[8] A. Luig, Diploma Thesis, BONN-IR-92-41, Bonn University (1992).
[9] S.P.H. Quinton et al., IEEE Trans. Nucl. Sci. NS-37 (1990) 2161; C.B. Brooks et al., Nucl. Instr. and Meth. A 283 (1989) 477.
[10] E. Badura and A.H. Walenta, Proc. Conf. on Electronics for Future Colliders, May 4–5, 1993; LeCroy Corp., Chestnut Ridge, NY, USA and Preprint Siegen University, SI-20-9-93 (1993); M. Rost and W. Weihs, 30 MHz hardwave digital filters for signals of the ZEUS Forward Tracking Detector, to be published in Nucl. Instr. and Meth.
[11] P.V. Walter and G. Mildner, IEEE Trans. Nucl. Sci. NS-32 (1985) 626.
[12] D. Schaile, O. Schaile and J. Schwarz, Nucl. Instr. and Meth. A 242 (1986) 247.
[13] H. Dabbous, Diploma Thesis, BONN-IR-88-43, Bonn University (1988).
[14] See e.g.: N.K. Bose, Digital Filters, Theory and Applications (North-Holland, 1986).
[15] M. Herzog, Diploma Thesis, BONN-IR-92-50, Bonn University (1992).
[16] R. Schattevoy, Diploma Thesis, BONN-IR-90-28, Bonn University (1990).
[17] M.P. Dobberstein, Doctoral Thesis, BONN-IR-90-51, Bonn University (1990).
[18] S. Gallego, Diploma Thesis, Universidad Autónoma de Madrid.
[19] J.E. Moyal, Philos. Mag. 46 (1955) 263.
[20] H. Breuker et al., Nucl. Instr. and Meth. A 260 (1987) 329.
[21] H. Drum et al., Nucl. Instr. and Meth. 176 (1980) 333.